The Astrophysical Journal, 932:72 (12pp), 2022 June 10 https://doi.org/10.3847/1538-4357/ac6b9c

Unraveling the Innermost Jet Structure of OJ 287 with the First GMVA + ALMA Observations

Guang-Yao Zhao[1], José L. Gómez[1], Antonio Fuentes[1], Thomas P. Krichbaum[2], Efthalia Traianou[1], Rocco Lico[1,3], Ilje Cho[1], Eduardo Ros[2], S. Komossa[2], Kazunori Akiyama[4,5,6], Keiichi Asada[7], Lindy Blackburn[6,8], Silke Britzen[2], Gabriele Bruni[9], Geoffrey B. Crew[4], Rohan Dahale[1,10], Lankeswar Dey[11], Roman Gold[12], Achamveedu Gopakumar[11], Sara Issaoun[8,13,34], Michael Janssen[2], Svetlana Jorstad[14,15], Jae-Young Kim[16,17,2], Jun Yi Koay[7], Yuri Y. Kovalev[18,19,2], Shoko Koyama[20,7], Andrei P. Lobanov[2], Laurent Loinard[21,22], Ru-Sen Lu[23,24,2], Sera Markoff[25,26], Alan P. Marscher[14], Iván Martí-Vidal[27,28], Yosuke Mizuno[29,30,31], Jongho Park[7,35], Tuomas Savolainen[32,33,2], and Teresa Toscano[1]

[1] Instituto de Astrofísica de Andalucía-CSIC, Glorieta de la Astronomía s/n, E-18008 Granada, Spain; gyzhao@iaa.es
[2] Max-Planck-Institut für Radioastronomie, Auf dem Hügel 69, D-53121 Bonn, Germany
[3] INAF-Istituto di Radioastronomia, Via P. Gobetti 101, I-40129 Bologna, Italy
[4] Massachusetts Institute of Technology Haystack Observatory, 99 Millstone Road, Westford, MA 01886, USA
[5] National Astronomical Observatory of Japan, 2-21-1 Osawa, Mitaka, Tokyo 181-8588, Japan
[6] Black Hole Initiative at Harvard University, 20 Garden Street, Cambridge, MA 02138, USA
[7] Institute of Astronomy and Astrophysics, Academia Sinica, 11F of Astronomy-Mathematics Building, AS/NTU No. 1, Sec. 4, Roosevelt Road, Taipei 10617, Taiwan, R.O.C.
[8] Center for Astrophysics | Harvard & Smithsonian, 60 Garden Street, Cambridge, MA 02138, USA
[9] INAF—Istituto di Astrofisica e Planetologia Spaziali, via Fosso del Cavaliere 100, I-00133 Roma, Italy
[10] Indian Institute of Science Education and Research Kolkata, Mohanpur, Nadia, West Bengal 741246, India
[11] Department of Astronomy and Astrophysics, Tata Institute of Fundamental Research, Mumbai 400005, India
[12] CP3-Origins, University of Southern Denmark, Campusvej 55, DK-5230 Odense M, Denmark
[13] Department of Astrophysics, Institute for Mathematics, Astrophysics and Particle Physics (IMAPP), Radboud University, P.O. Box 9010, 6500 GL Nijmegen, The Netherlands
[14] Institute for Astrophysical Research, Boston University, 725 Commonwealth Ave., Boston, MA 02215, USA
[15] Astronomical Institute, St. Petersburg University, Universitetskij pr., 28, Petrodvorets,198504 St.Petersburg, Russia
[16] Department of Astronomy and Atmospheric Sciences, Kyungpook National University, Daegu 702-701, Republic of Korea
[17] Korea Astronomy and Space Science Institute, Daedeok-daero 776, Yuseong-gu, Daejeon 34055, Republic of Korea
[18] Lebedev Physical Institute of the Russian Academy of Sciences, Leninsky prospekt 53, 119991 Moscow, Russia
[19] Moscow Institute of Physics and Technology, Institutsky per. 9, Dolgoprudny, Moscow region, 141700, Russia
[20] Niigata University, 8050 Ikarashi-nino-cho, Nishi-ku, Niigata 950-2181, Japan
[21] Instituto de Radioastronomía y Astrofísica, Universidad Nacional Autónoma de México, Morelia 58089, México
[22] Instituto de Astronomía, Universidad Nacional Autónoma de México, CdMx 04510, México
[23] Shanghai Astronomical Observatory, Chinese Academy of Sciences, 80 Nandan Road, Shanghai 200030, People's Republic of China
[24] Key Laboratory of Radio Astronomy, Chinese Academy of Sciences, Nanjing 210008, People's Republic of China
[25] Anton Pannekoek Institute for Astronomy, University of Amsterdam, Science Park 904, 1098 XH, Amsterdam, The Netherlands
[26] Gravitation and Astroparticle Physics Amsterdam (GRAPPA) Institute, University of Amsterdam, Science Park 904, 1098 XH, Amsterdam, The Netherlands
[27] Departament d'Astronomia i Astrofísica, Universitat de València, C. Dr. Moliner 50, E-46100 Burjassot, València, Spain
[28] Observatori Astronòmic, Universitat de València, C. Catedrático José Beltrán 2, E-46980 Paterna, València, Spain
[29] Tsung-Dao Lee Institute, Shanghai Jiao Tong University, Shengrong Road 520, Shanghai, 201210, People's Republic of China
[30] School of Physics and Astronomy, Shanghai Jiao Tong University, 800 Dongchuan Road, Shanghai, 200240, People's Republic of China
[31] Institut für Theoretische Physik, Goethe-Universität Frankfurt, Max-von-Laue-Straße 1, D-60438 Frankfurt am Main, Germany
[32] Aalto University Department of Electronics and Nanoengineering, PL 15500, FI-00076 Aalto, Finland
[33] Aalto University Metsähovi Radio Observatory, Metsähovintie 114, FI-02540 Kylmälä, Finland
Received 2022 March 21; revised 2022 April 26; accepted 2022 April 27; published 2022 June 16

Abstract

We present the first very long baseline interferometric (VLBI) observations of the blazar OJ 287 carried out jointly with the Global Millimeter VLBI Array (GMVA) and the phased Atacama Large Millimeter/submillimeter Array (ALMA) at 3.5 mm on 2017 April 2. The participation of phased ALMA has not only improved the GMVA north–south resolution by a factor of ∼3, but has also enabled fringe detections with signal-to-noise ratios up to 300 at baselines longer than 2 Gλ. The high sensitivity has motivated us to image the data with newly developed regularized maximum likelihood imaging methods, revealing the innermost jet structure with unprecedentedly high angular resolution. Our images reveal a compact and twisted jet extending along the northwest direction, with two bends within the inner 200 μas, resembling a precessing jet in projection. The component at the southeastern end shows a compact morphology and high brightness temperature, and is identified as the VLBI core. An extended jet feature that lies at ∼200 μas northwest of the core shows a conical shape, in both total and linearly polarized

[34] NASA Hubble Fellowship Program, Einstein Fellow.
[35] EACOA Fellow.

intensity, and a bimodal distribution of the linear polarization electric vector position angle. We discuss the nature of this feature by comparing our observations with models and simulations of oblique and recollimation shocks with various magnetic field configurations. Our high-fidelity images also enabled us to search for possible jet features from the secondary supermassive black hole (SMBH) and test the SMBH binary hypothesis proposed for this source.

Unified Astronomy Thesaurus concepts: Very long baseline interferometry (1769); AGN host galaxies (2017); Radio jets (1347); Jets (870); Supermassive black holes (1663); Radio continuum emission (1340)

1. Introduction

The BL Lac–type object OJ 287 ($z = 0.306$; Stickel et al. 1989) is a well-studied low synchrotron peaked BL Lac object that has attracted great interest, as it shows quasiperiodic optical outbursts with a cycle of about 12 yr. These outbursts appear to come in pairs, with separations of one to two years, and they have been suggested to originate due to the presence of a supermassive binary black hole (SMBBH) system at its center (e.g., Sillanpää et al. 1988; Lehto & Valtonen 1996). According to this model, the observed quasiperiodic double-peaked optical outbursts are triggered when the secondary supermassive black hole (SMBH) impacts the accretion disk of the primary in its orbit. Further advances of this model have accounted for general relativistic effects, and the parameters have also been further constrained with follow-up observations (e.g., Valtonen et al. 2008, 2011; Dey et al. 2018). The model requires a compact binary with a major axis of the orbit of 0.112 pc (corresponding to an angular scale of $\sim$26 μas; e.g., Valtonen et al. 2008), featuring a very massive primary black hole (BH) of $1.8 \times 10^{10} M_{\odot}$, and a secondary of $1.5 \times 10^{8} M_{\odot}$ (e.g., Valtonen et al. 2012; Dey et al. 2018). This model is not only successful in reproducing the observed light curves of OJ 287, but also in predicting impact outbursts that have later been confirmed by observations (e.g., Valtonen et al. 2006, 2016; Laine et al. 2020; Komossa et al. 2020). Independent of the binary model of OJ 287, the dedicated multiwavelength observations and modeling of the OJ 287 (MOMO) project has led to the discovery of several bright flare events and long-lasting deep fades, while the monitoring spectroscopy over the last two decades has established OJ 287 as one of the most spectrally variable blazars in the soft X-ray band (e.g., Komossa et al. 2017, 2021a, 2021b, 2021c).

Another observational signature of OJ 287 is that the position angle (PA) of the parsec-scale jet was found to be "wobbling" by previous very long baseline interferometric (VLBI) observations (e.g., Tateyama & Kingham 2004; Agudo et al. 2012; Cohen 2017; Britzen et al. 2018). Such changes in the inner jet PA could also be explained by the SMBBH model (e.g., Dey et al. 2021), but alternative models cannot be fully ruled out. For instance, Agudo et al. (2012) suggest instabilities coupled to the accretion disk as the likely origin of the nonperiodic changes in the inner jet orientation. Britzen et al. (2018) suggest that the flux variation could be explained by viewing angle changes and the Doppler beaming effects of a precessing jet. The precession could be driven by either the binary motion (e.g., Dey et al. 2021) or the Lense–Thirring effect due to the misalignment between the BH spin and the accretion disk (e.g., Liska et al. 2018; Chatterjee et al. 2020).

The massive central BH, the relatively low redshift, and the bright relativistic jet close to the line of sight also make OJ 287 one of the nearest high-luminosity active galactic nuclei in which the magnetic launching and acceleration of jets can be studied through high-resolution VLBI observations. Two competing scenarios have been proposed for the formation of relativistic jets. The main difference between them is whether the magnetic fields are twisted by the rotational energy of the BH (Blandford & Znajek 1977) or its accretion disk (Blandford & Payne 1982). It is also possible that both mechanisms are at work (e.g., Chiaberge et al. 2000). In the innermost region of the jet, the plasma flow is accelerated and collimated in the presence of a spiral magnetic field, while the jet expands in width and propagates downstream into the interstellar space. The disruption of the accretion flow and the interaction with the ambient medium often result in the formation of moving and standing shocks. The detailed process of jet formation, acceleration, and collimation remains unclear, as extremely high angular resolution is required to probe into the innermost region in the vicinity of the central BH.

High-resolution VLBI observations are ideal for probing the compact structure near the central engine. Previous VLBI observations of OJ 287 have provided key information on the parsec-scale structure and the dynamics of the jet (e.g., Cohen 2017; Hodgson et al. 2017; Britzen et al. 2018). In particular, Gómez et al. (2022) recently presented 22 GHz images of OJ 287 with unprecedented angular resolution for the source, obtained with RadioAstron space–ground VLBI observations. The images revealed a progressive bending of the inner jet with increasing angular resolution, by comparison with multiband ground-based VLBI images. The inner jet components show high brightness temperatures that exceed the inverse Compton limit, indicating strong Doppler boosting in the jet. The polarized images show electric vector position angles (EVPAs) aligned with the jet axis, which indicates that the jet has a predominantly toroidal magnetic field. Multi-frequency analysis shows hints of a rotation measure gradient across the jet, which suggests that the VLBI core is threaded by a helical magnetic field.

VLBI observations at wavelengths shorter than 7 mm have the potential to probe areas closer to the central engine that are optically thick at lower frequencies (see, e.g., Boccardi et al. 2017). Previous VLBI observations at 3.5 mm with the Global Millimeter VLBI Array (GMVA) show the existence of quasi-stationary components and changes in the morphology and PA in the innermost jet region (e.g., Hodgson et al. 2017). However, most of the previous GMVA observations are limited in sensitivity, due to typically shorter atmospheric coherence times, lower antenna efficiencies, and thus higher system-equivalent flux densities compared to longer wavelengths. The participation of large sensitive stations in millimeter-VLBI observations is desirable, together with further developments of the instruments and calibration methods (e.g., Rioja & Dodson 2011; Rioja et al. 2017; Zhao et al. 2018).

In this paper, we present the first VLBI observations of OJ 287 with the GMVA and phased Atacama Large Millimeter/submillimeter Array (ALMA) on 2017 April 2. These observations are accompanied by a multiwavelength campaign,

including the first 1.3 mm observation of the source with the Event Horizon Telescope (EHT; Event Horizon Telescope Collaboration et al. 2019a), the results of which will be presented in a forthcoming paper. The campaign was carried out during a major outburst event of OJ 287 in 2016–17, with the largest X-ray outburst recorded so far (Komossa et al. 2017, 2021c) and the first very-high-energy (VHE) flare detection (Mukherjee & VERITAS Collaboration 2017).

We summarize the details of the GMVA + ALMA observations and the methods that we use to calibrate, image, and analyze the data in Section 2. We present our observational results, including total intensity and linear polarization images in Section 3. In Section 4, we discuss the nature of the components in the jet and possible constraints on the theoretical models, followed by a summary in Section 5.

2. Observations and Data Analysis

In this section, we describe the details of our 3.5 mm observations of OJ 287 with GMVA + ALMA, the data calibration procedure, and the methods used to obtain subparsec-scale images of OJ 287.

2.1. Observations

We carried out high-resolution VLBI observations toward OJ 287 at 3.5 mm with GMVA on 2017 April 2. These observations mark the first VLBI observations with the phased ALMA, which consists of 37 ALMA antennas and is equivalent to a 70 meter dish (Event Horizon Telescope Collaboration et al. 2019a). The participating stations also include eight Very Long Baseline Array (VLBA) stations and five European stations (Effelsberg, IRAM-30 m, Metsähovi, Onsala, Yebes-40m). The on-source time was around 375 minutes between UT 17 and UT 7 the next day (April 3).

Most stations had good or typical weather conditions during the observation, except for the VLBA Maunakea and Pie Town stations, which resulted in few fringe detections with limited signal-to-noise ratio (S/N) on the baselines to these two stations. No fringes were found on the baselines to Metsähovi, due to a faulty backend setup. All data were recorded in full polarization mode, with most stations recording on a circular polarization basis, while the ALMA data were converted from a mixed linear–circular basis to circular polarization mode using `PolConvert` (Martí-Vidal et al. 2016). The Yebes-40 m telescope recorded only left-handed circular polarization (LCP). The bandwidths and frequency ranges recorded are not the same for all stations.[36] Only the common frequency ranges among all participating stations are used in later processing.

2.2. Data Reduction

Data correlation was performed with the DiFX correlator (Deller et al. 2007) at the Max-Planck-Institut für Radioastronomie in Bonn, Germany. The final correlated data have a total bandwidth of 232 MHz, which was further divided into four 58 MHz intermediate frequency (IF) bands.

The postcorrelation data set was then processed with the `ParselTongue` (Kettenis et al. 2006) *AIPS* (Greisen 2003) interface for fringe fitting and a priori amplitude calibration.

[36] The recorded bandwidth for each station is as follows: ALMA 32×62.5MHz, VLBA 2×128MHz, and most European stations 1×512MHz.

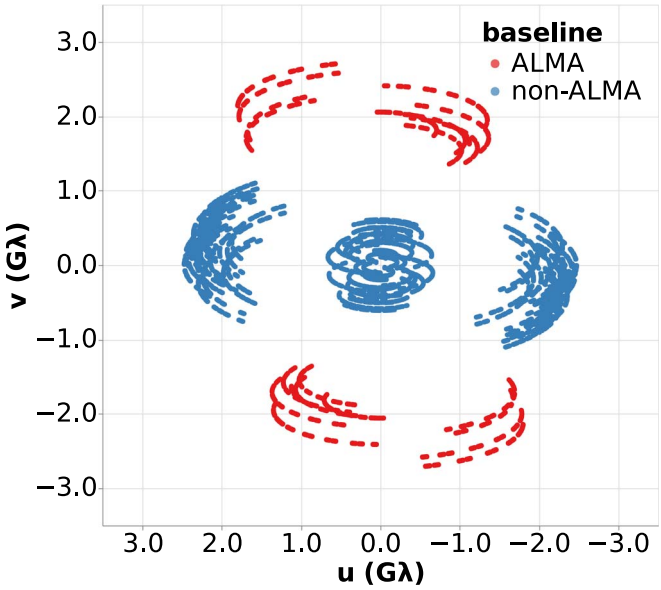

Figure 1. (u,v)-coverage of the fringe-fitted interferometric visibilities of OJ 287, observed with GMVA + ALMA on 2017 April 2 at 86 GHz. The baselines to ALMA are plotted in red and the other GMVA baselines are plotted in blue.

We first performed parallactic angle correction with the *AIPS* task CLCOR[37], and manual phase calibration using short segments of data to remove the instrumental phase offset between the different IFs. We then performed a global fringe fitting of the data using the task FRING, with a solution interval of 10 s and subintervals down to 2 s, and by integrating over the whole 232 MHz bandwidth and averaging parallel-hand polarizations (RR and LL).

The (u,v)-coverage toward OJ 287 for all baselines with fringe detections is shown in Figure 1. We note that the participation of ALMA has provided an increase in the north–south resolution by a factor of ∼3 for observations of OJ 287. ALMA has also significantly improved fringe detection due to its high sensitivity (see Figure 2) with the maximum fringe S/N reaching ∼350 at baselines longer than 1.5 Gλ.

A priori amplitude calibration was performed in *AIPS* with the task APCAL, by multiplying the system temperatures ($T_{\rm sys}$) and gain curves of each antenna. Opacity corrections were applied to stations that measure system temperatures with the noise diode method (VLBA and Effelsberg). For ALMA, IRAM-30 m, and Yebes-40 m, the $T_{\rm sys}$ measurements were performed using the hot/cold method, and therefore already included opacity correction. The ALMA $T_{\rm sys}$ values have also taken into account the phasing efficiencies derived during the quality assurance and `PolConvert` processes (e.g., Goddi et al. 2019). The cross-hand phase and delay offsets of the reference station were calibrated using the *AIPS* procedure VLBACPOL.

After the *AIPS* calibration, the data were averaged in time (with an interval of 15 s) and frequency (with all channels within each IF averaged) for further processing.

[37] We note that the mount types for IRAM-30 m (Nasmyth-Left) and Yebes-40 m (Nasmyth-Right) are different from the rest of the antennas in the array (altitude–azimuth). The Yebes-40 m data were not used for polarimetric analysis, as they were only recorded in LCP.

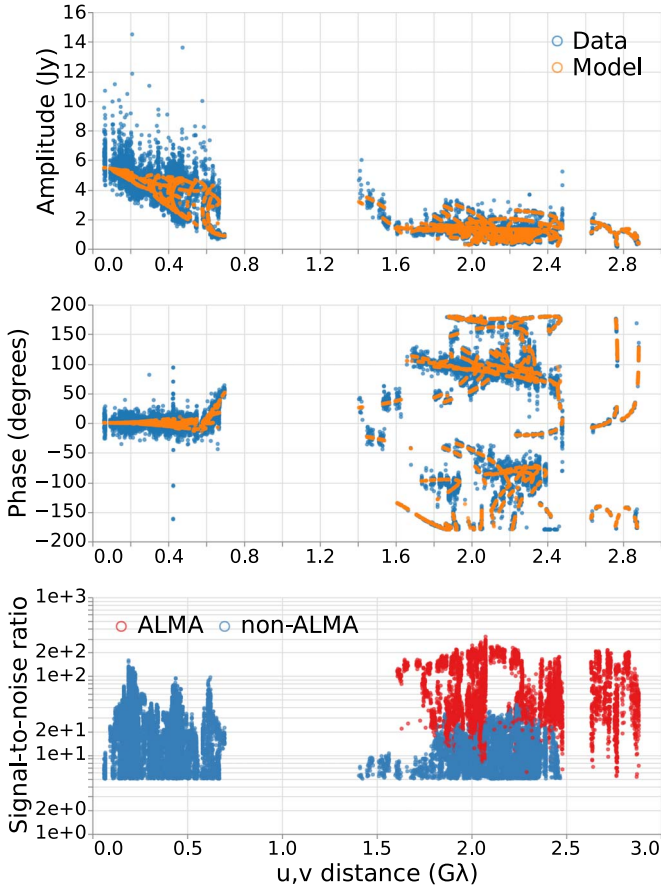

Figure 2. Self-calibrated visibility amplitudes (top) and phases (middle) as a function of (u,v)-distance of the GMVA + ALMA observations of OJ 287 on 2017 April 2 at 86 GHz. The data were averaged every 15 s and all channels in each IF are averaged. Overplotted in orange are the fits to the data of the reconstructed image obtained with `SMILI`. The bottom panel shows the fringe S/N as a function of (u,v)-distance, with the data on the ALMA baselines plotted in red and the other baselines in blue.

2.3. Imaging and Model Fitting

We performed the imaging and self-calibration of the data independently with three different imaging softwares: `DIFMAP`, `eht-imaging`, and `SMILI`. `DIFMAP` is the software commonly used for the conventional CLEAN method for interferometric imaging (Shepherd et al. 1995). It interactively establishes a collection of point-source models from the inverse Fourier transform of the visibilities, i.e., the dirty map. CLEAN windows, which define the regions to search for CLEAN components, are used during our imaging process. Phase-only self-calibration is performed after each step of cleaning. Amplitude and phase self-calibration is performed once a good fit to the visibilities has been established through multiple steps of cleaning and phase self-calibration. We repeat the clean and self-calibration loops several times during our imaging process by gradually decreasing the solution interval of the amplitude and phase self-calibration. On the other hand, the regularized maximum likelihood (RML) methods, employed by the `eht-imaging` (Chael et al. 2016, 2018) and `SMILI` (Akiyama et al. 2017) libraries, reconstruct images by minimizing an objective function, which is a weighted combination of χ^2 of the data and various regularizer terms. The data terms may include closure quantities (closure phases and amplitudes; e.g., Thompson et al. 2017), visibility amplitudes, and complex visibilities. Common regularizers include the maximum entropy (e.g., Chael et al. 2018), the ℓ_1-norm (e.g., Honma et al. 2014; Akiyama et al. 2017), the total variation (TV), and the total squared variation (TSV) of the brightness (e.g., Kuramochi et al. 2018). With RML methods, it is possible to achieve an angular resolution a few times finer than the nominal interferometric beam (e.g., Akiyama et al. 2017; Event Horizon Telescope Collaboration et al. 2019b). During our imaging process with `eht-imaging` and `SMILI`, we started with a Gaussian prior image and reconstructed images with only the closure quantities, or a combination of closure quantities and low-weighted visibility amplitudes. After a few iterations of imaging and self-calibrating, we included full complex visibilities in the optimization process, further constraining the reconstructed images. To determine the best set of regularizer combinations, we surveyed a range of different weights of each regularizer, in a total of ∼128 combinations, and selected the one that resulted in the best fit to the closure quantities.

After the imaging of the total intensity, we estimated the instrumental polarimetric leakage (known as D-terms) for each station, using the self-calibrated data of OJ 287. This process was carried out independently with two pipelines: the *AIPS* task LPCAL and the `eht-imaging` library, each based on a particular self-calibrated data set generated during the total intensity imaging process, i.e., `DIFMAP` and `eht-imaging`, respectively. Both approaches provide consistent values of D-terms. Details of the leakage calibration are described in the Appendix. The polarization imaging of the LPCAL processed data was carried out with `DIFMAP`. With `eht-imaging`, the imaging was performed iteratively with the D-terms calculation. The calibration of the absolute orientation of the EVPAs was performed through comparison with the ALMA array data (Goddi et al. 2021).

We also carried out nonimaging analysis of the data to measure the properties of the jet. We performed circular Gaussian model fitting to the `SMILI` self-calibrated visibility data with `DIFMAP`. The results indicated that the jet structure could be represented by four Gaussian components. We labeled the components following the convention described in Gómez et al. (2022). The total flux, size, and position offset with respect to the core (the component at the southeastern end of the jet; see Section 3 below) of all the components are listed in Table 1. The uncertainties of the fitted parameters are derived following the equations outlined in Nair et al. (2019).

3. Results

3.1. Jet Morphology

Figure 3 shows the total intensity maps of OJ 287 obtained with our GMVA + ALMA observations, achieving the highest angular resolution to date of the source at the wavelength of 3.5 mm. The imaging results are consistent across different imaging methods (CLEAN and RML). Under the nominal resolution, the jet appears to consist of three major features, extending along the southeast to northwest direction. We denote the three features as the components C0, C1, and C2, as shown in the bottom right panel of Figure 3.

Component C0, which lies at the southern end of the jet, is compact and shows the highest brightness temperature (Table 1). This feature is more likely to be the VLBI core at 3.5 mm. The component C2 has the highest flux density among

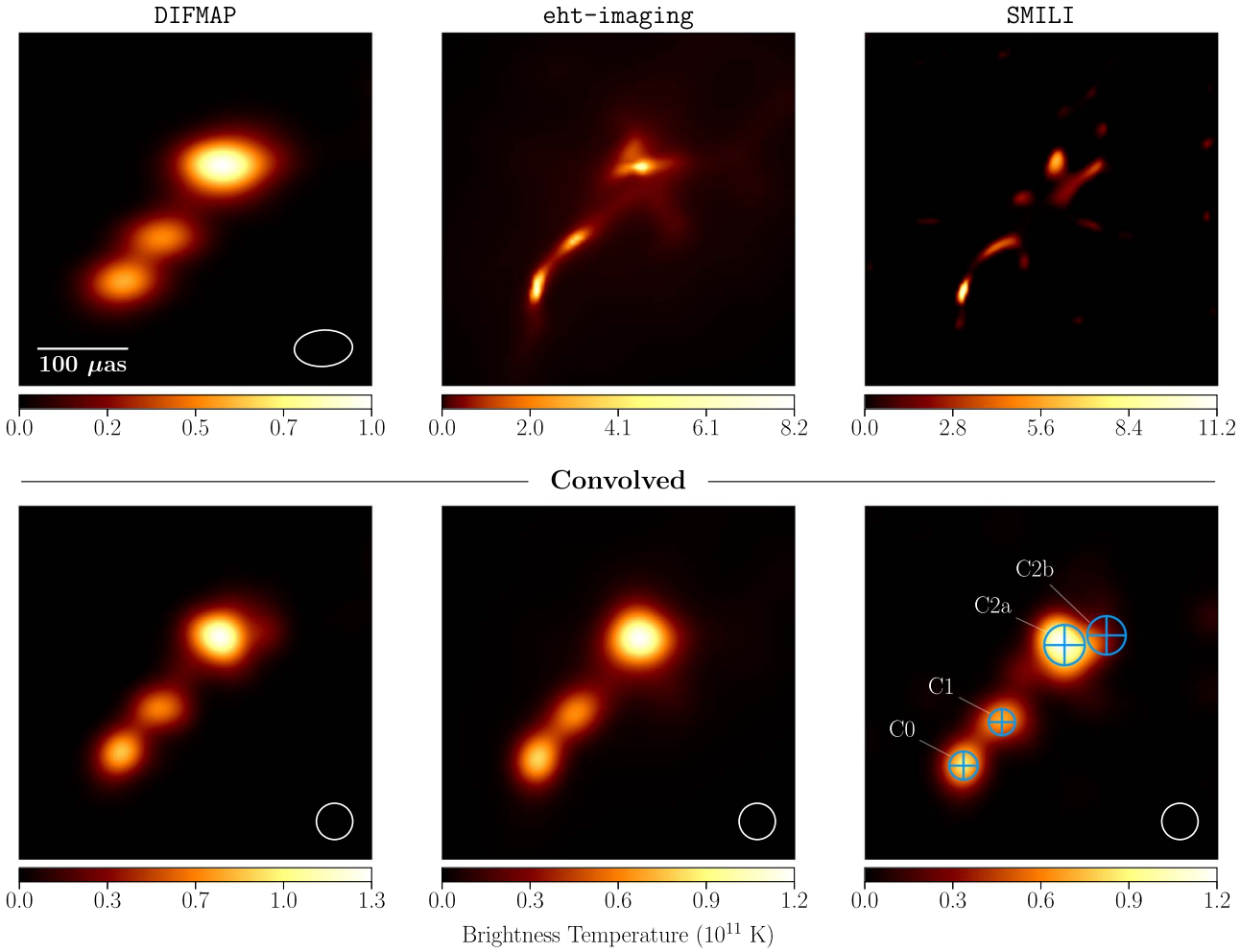

Figure 3. From left to right: total intensity maps of OJ 287 at 3.5 mm obtained with GMVA + ALMA observations on 2017 April 2, reconstructed with `DIFMAP`, `eht-imaging`, and `SMILI`, respectively. The *x*-axis and *y*-axis in each image represent the right ascension and declination axes on the sky, respectively. The `DIFMAP` image is convolved with the natural-weighted beam size of the array, which is 64 × 40 μas at a PA of −86°. For the `DIFMAP`, `eht-imaging`, and `SMILI` images, respectively, the reduced χ^2 of the closure phases is: 1.21, 1.22, and 1.19; and that of the log closure amplitudes is: 1.18, 1.22, and 1.08. The second row shows the same images, but convolved with a circular beam of 40 μas. The bottom right panel shows the model-fitted circular Gaussian components overlaid on the convolved SMILI total intensity map. The flux, location, and size of each component are listed in Table 1.

Table 1
Model Fitting Parameters of OJ 287 with GMVA + ALMA on 2017 April 2

Comp Name (1)	S (Jy) (2)	r (μas) (3)	PA ($^\circ$) (4)	FWHM (μas) (5)	$T_b^{\rm obs}$ (10^{10} K) (6)
C0	1.25 ± 0.13	0.0	0.0	31.1 ± 2.4	21.2 ± 4.1
C1	0.96 ± 0.10	63.9 ± 2.4	-41.5 ± 2.2	28.9 ± 2.4	18.8 ± 3.9
C2a	2.49 ± 0.25	172.9 ± 2.4	-40.0 ± 0.8	44.4 ± 2.5	20.6 ± 3.1
C2b	0.51 ± 0.05	212.7 ± 3.5	-47.7 ± 0.9	42.5 ± 4.6	4.7 ± 1.2

Note. Columns from left to right: (1) Component ID; (2) Flux density; (3) Radial distance from the core component (C0); (4) Position angle; (5) Component FWHM; and (6) Observed brightness temperature.

the three components. This feature shows complex substructures under the fine resolution of the RML images (Figure 3, top middle and top right panels). We see hints of the jet bending and extending toward the western direction downstream of C2. This bend is more obvious in the lower-frequency maps which are more sensitive to the extended lower-brightness regions despite the lower angular resolutions (e.g., Cohen 2017; Jorstad et al. 2017). The downstream jet is largely resolved out and not well constrained in our high-resolution images, because of their steep spectra and extended structure. Our higher-resolution images reveal for the first time the twisted morphology of the innermost, ultracompact jet region. The first bending occurs between C0 and C1, with the jet axis gradually changing from north to northwest

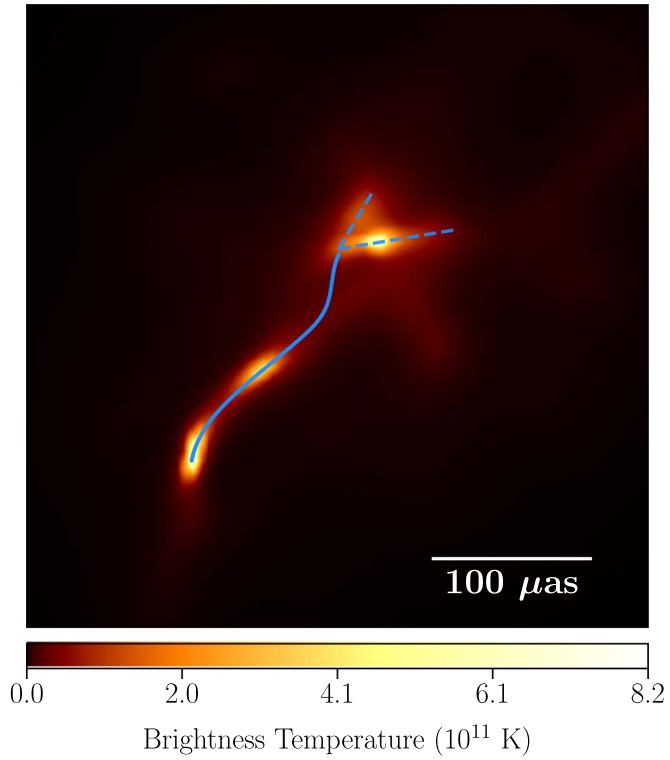

Figure 4. The continuous blue line traces the ridgeline of the inner jet of OJ 287, overplotted on the super-resolution image reconstructed with `eht-imaging`. The dashed blue lines represent the conical structure of the C2 component.

(clockwise). We also see hints of a subsequent bending occurring downstream of C1, where the jet axis turns in the counterclockwise direction.

The three-component structure is also consistent with the recent 22 GHz RadioAstron space–ground VLBI observations of OJ 287 made at a similar resolution (Gómez et al. 2022). However, a PA difference of ∼50° in the inner jet can be found when comparing with the RadioAstron image obtained in 2014. Such a difference could be attributed to the variation in the PA over ∼ 3 yr. A detailed analysis of the inner jet PA variation on a yearly scale, and a comparison with theoretical predictions, will be presented in a forthcoming paper (G-Y. Zhao et al., in preparation).

In order to quantify the PA evolution along the jet, we fit the jet ridgeline on the `eht-imaging` map. First, we transform the image to polar coordinates centered on the jet origin, then slice it transversely. For each slice, we store the flux density peak position, then transform them back to Cartesian coordinates. Thus, we obtain a collection of positions tracing the jet axis between C0 and C2. The results are presented in Figure 4, where we also show a sketch tracing the conical structure of C2 in the figure. The jet axis near C0 extends along a PA of ∼−15°, decreases to ∼−50° at C1, and then starts to increase again near C2. A similar trend can also be found in the `SMILI` image.

3.2. Brightness Temperatures

We investigate the brightness temperature of the OJ 287 jet using two independent approaches. (1) We calculate the observed brightness temperature of each Gaussian component from the model fitting results, using the following equation

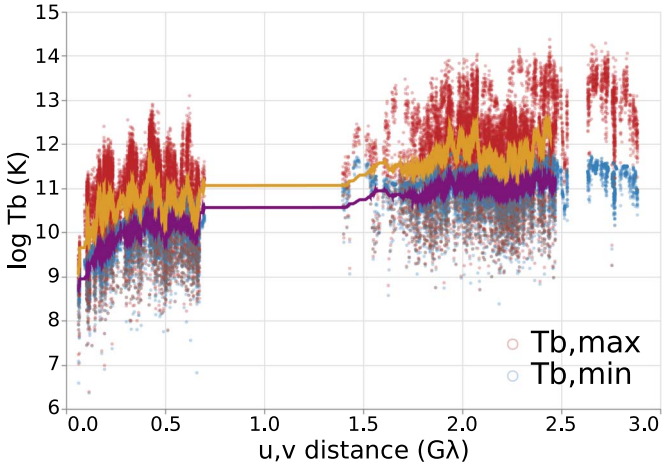

Figure 5. Visibility-based brightness temperature estimates of OJ 287 at 86 GHz, using the method described in Lobanov (2015). The red and blue dots are the values of $T_{\rm b,max}$ and $T_{\rm b,min}$, respectively. The orange and purple curves are the rolling means of the $T_{\rm b,max}$ and $T_{\rm b,min}$ values.

(e.g., Tingay et al. 2002):

$$T_{\rm b}^{\rm obs} = 1.22 \times 10^{12} \frac{S}{\theta_{\rm obs}^2 \nu^2}, \quad (1)$$

where S is the component flux density in Jy, $\theta_{\rm obs}$ is the size of the emitting region in mas, and ν is the observing frequency in GHz. (2) We calculate the minimum and maximum brightness temperature directly from the visibilities, using the method described in Lobanov (2015). The model fitting results, which are listed in Table 1, show the observed brightness temperature of the jet components at 86 GHz ranges from 10^{10} to 10^{11} K. This is in agreement with the values calculated from the visibility amplitudes, as shown in Figure 5. The brightness temperature values agree quantitatively with the typical values at the same frequency band (e.g., Lee et al. 2008; Nair et al. 2019). The 86 GHz brightness temperatures are about one order of magnitude lower compared to those at 22 GHz obtained from the RadioAstron results (Gómez et al. 2022). This can be attributed to differences in the intrinsic brightness and opacity between the two frequencies.

We estimate the intrinsic brightness temperature, $T_{\rm b}^{\rm int}$, by (e.g., Gómez et al. 2016):

$$T_{\rm b}^{\rm int} = (1+z)\delta^{-1} T_{\rm b}^{\rm obs}, \quad (2)$$

where δ stands for the Doppler factor. We adopt the value of the latest estimate based on the proper motion of moving components from the VLBA-BU-BLAZAR monitoring program, $\delta = 8.6 \pm 2.8$ (Weaver et al. 2022). This gives the intrinsic brightness temperature values $T_{\rm b,C0}^{\rm int} = (3.2 \pm 1.7) \times 10^{10}$ K, $T_{\rm b,C1}^{\rm int} = (2.8 \pm 1.4) \times 10^{10}$ K, $T_{\rm b,\,C2a}^{\rm int} = (3.1 \pm 1.4) \times 10^{10}$ K, and $T_{\rm b,\,C2b}^{\rm int} = (0.7 \pm 0.4) \times 10^{10}$ K, for each component, respectively. These values fall below the equipartition value of $\sim 5 \times 10^{10}$ (Readhead 1994), indicating possible magnetic dominance in the innermost jet. However, this is quite uncertain, as the errors in the Doppler factor and brightness temperature values are large.

3.3. Polarization

We perform polarimetric imaging of the instrumental polarization calibrated data with CLEAN and `eht-imaging`

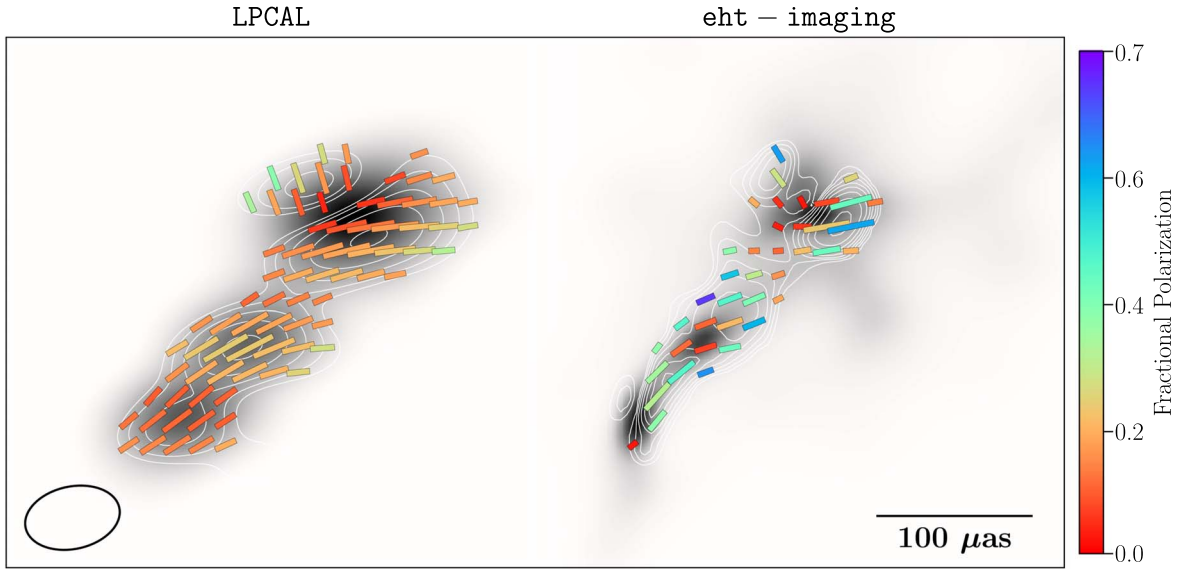

Figure 6. Polarized images of OJ 287 produced by the LPCAL + CLEAN method (left) and the RML imaging method `eht-imaging` (right). The total intensity image is shown in grayscale. The contours represent the linearly polarized flux density. The ticks show the orientations of the EVPAs, where the lengths indicate the polarization intensity magnitudes, and the colors represent the fractional polarization. Only the LPCAL + CLEAN image is convolved with the beam, shown in the bottom left corner.

independently. The corresponding images are shown in Figure 6. Our images show that the overall degree of polarization of OJ 287 is ∼8%, which is in quantitative agreement with the ALMA array results of 8.8% presented in Goddi et al. (2021). The EVPAs extend mostly along the mean jet axis, which suggests that the magnetic field in the jet has a predominant toroidal component. Again, the image reconstructed by `eht-imaging` shows a fine structure, because of the super-resolution that is naturally achieved by the forward-modeling method. However, even in the CLEAN image, which is convolved with the nominal beam, we see a remarkable polarimetric structure in the inner jet. The overall structure is consistent between the two images that have been reconstructed independently with different approaches. We notice that the apparent difference in the fractional polarization between the two maps is due to the fact that the CLEAN images are convolved with the nominal beam. The overall degree of polarization and the EVPA distributions agree well between the two images.

Of the several jet components, C0 shows the lowest fractional polarization of ∼5%, as measured from the `eht-imaging` map. This further supports this component being the jet core, which is usually depolarized (e.g., Lister & Homan 2005). C1 exhibits a high level of polarization (∼16%), which indicates that the magnetic field is more ordered in this region. C2 shows a conspicuous polarimetric structure, which can be further divided into two subcomponents, with the EVPAs lying perpendicular to each other. The EVPAs in the upper subcomponent also lie perpendicular to the direction along which the brightness extends, while in the bottom subcomponent, they lie nearly in parallel. The degrees of polarization are ∼7% and ∼13% in the upper and lower subcomponents, respectively. These substructures are clearly seen in both the `eht-imaging` and CLEAN images.

4. Discussion

4.1. Nature of the C2 Region

Our GMVA + ALMA observations have revealed a remarkable structure of the inner jet of OJ 287 because of the improved (u,v)-coverage and high sensitivity. In particular, the C2 component shows a complex conical structure in both total and linearly polarized intensity, and a bimodal distribution in the EVPAs. Previous multi-epoch observations have shown that this component is nearly stationary (e.g., Hodgson et al. 2017; Jorstad et al. 2017; Lico et al. 2022). In the following, we discuss the possible nature of this component.

Oblique shocks could result from the jet striking a cloud of interstellar media. Under the precessing jet model, this would naturally occur for some period, as the jet sweeps through the ambient material. Since the location of C2 coincides with where the jet bends, the northeastern section of C2 could be interpreted as an oblique shock on one side of the jet. The oblique shock is in a plane making a small angle to the jet boundary on the northeast side. The flow is then bent by the shock toward the west. The magnetic field could become compressed to strengthen the component nearly parallel to the jet. Therefore, the EVPAs on the northeast side are roughly perpendicular to the jet. The southwestern section of C2 could then just be the main jet after the bend, with the magnetic field transverse to the jet direction at that point, as usual for a BL Lac object.

Conical shock waves can be formed when there is a pressure imbalance between the jet plasma and the ambient medium. The properties of shocks in relativistic jets have been explored by numerical and semidynamical simulations. Gomez et al. (1995) carried out relativistic hydrodynamics simulations of a parsec-scale jet surrounded by an ambient medium with constant or decreasing pressure. The simulations confirmed the existence of stationary components associated with recollimation shocks. Gómez et al. (1997) simulated the

interactions of standing shocks and relativistically moving perturbations propagating down the stable jet, and found that the shock could enhance the emission of the moving feature and the stationary component could be temporarily "dragged" downstream. Further simulations of the interactions between recollimation shocks and traveling shocks are presented in Fromm et al. (2016), based on the observations presented in Fromm et al. (2011, 2013a, 2013b, 2015), for the particular case of CTA 102. Various configurations of the upstream magnetic field components have also been included in subsequent numerical simulations (e.g., Broderick & McKinney 2010; Porth et al. 2011; Fuentes et al. 2018). In particular, Mizuno et al. (2015) studied kinematically dominated jets with different magnetic field configurations, including axial, toroidal, and helical, based on a relativistic magnetohydrodynamics (RMHD) simulation code. Fuentes et al. (2018) characterized the properties of recollimation shocks in RMHD simulations of jets at the parsec scale as a function of the dominant type of energy: internal, kinetic, or magnetic. By solving the radiative transfer equations for synchrotron radiation, using these simulations as inputs, they analyzed the total intensity and linear polarization signatures imprinted in the stationary components associated with these shocks. Fuentes et al. (2021) extended the analysis to RMHD jet models threaded by helical magnetic fields with larger magnetic pitch angles, and also explored the effect of different nonthermal particle populations on the polarimetric properties of stationary features and the overall observed synchrotron radiation.

On the other hand, Cawthorne & Cobb (1990) established a semidynamical model, assuming only that the shock front is emitting, and found that conical shock waves could result in polarization angles that were either parallel or perpendicular to the jet axis. This model also only considered random magnetic fields in the upstream jet. In Cawthorne (2006), a poloidal magnetic field component was added to the model, and the results can well explain the observed polarization of the knot K1 in 3C 380. Furthermore, Cawthorne et al. (2013) extended this model to include a paired collimating and decollimating shock, and the predicted EVPAs could successfully describe the observational results of the BL Lac object $1803+784$.

Comparing our observational results of C2 with the numerical and semidynamical studies, we find that the conical shape of the emitting region is quite consistent between our observations and the simulations. Numerical simulations predict a series of stationary shocks along the jet that can be triggered by a pressure imbalance between the jet and the external medium. The reason that we find only one conical-shaped component is most likely the adiabatic expansion of the jet. As also shown in Gomez et al. (1995), with decreasing pressure downstream of the jet, the intensity of the stationary components gradually decreases and the separation between the components increases, so the downstream shocks may be too faint and become undetectable at our observing frequency. Regarding the polarized emission, the semidynamical simulations show different EVPA distributions across the cone. However, the EVPA pattern is more symmetric with respect to the cone axis. The numerical simulations also show that the EVPA pattern will depend on the upstream magnetic field configuration and the viewing angle (e.g., Mizuno et al. 2015; Gómez et al. 2016; Fuentes et al. 2021). Fuentes et al. (2021) pointed out that jets with a large magnetic pitch angle, i.e., threaded by a helical magnetic field dominated by its toroidal component, can exhibit a bimodal EVPA distribution around recollimation shocks for small viewing angles. This EVPA configuration could imply a sign flip of the Stokes $\mathcal{Q}$ parameter that leads to an EVPA flip, which then results in a dip in the linearly polarized emission, as we observe in the C2 component from the reconstructed polarimetric images.

Alternative to the standing shock scenario, the observed properties of the C2 component could be a result of geometric effects due to the bending of the jet axis toward the line of sight. With a decreasing viewing angle, the enhanced Doppler boosting could amplify the emission in this region and make C2 the brightest component in the inner jet. If the viewing angle becomes smaller than the jet opening angle, the bimodal distribution of the EVPAs could be produced by the existence of helical magnetic fields in the jet, as the direction of the projected magnetic field is different across the component (Fuentes et al. 2021). This scenario is supported by previous observations that revealed the existence of bending around C2 (e.g., Hodgson et al. 2017; Jorstad et al. 2017; Gómez et al. 2022). However, it is difficult to explain the conical shape of the emission region with this assumption.

Moreover, by means of multi-epoch GMVA observations, Lico et al. (2022) identified a new jet feature in the region of C2, in a quasi-concurrent GMVA observing epoch. The authors argued that the passage of this new jet component through the stationary feature at 0.1 mas core separation (i.e., C1) triggered the high-energy outburst during 2016–2017 (Komossa et al. 2017, 2021a), including the faint VHE flare detected in February 2017 (Mukherjee & VERITAS Collaboration 2017)[38] and then moved down to the C2 jet region at the time of these observations. In this scenario, the C2 component in our observations could correspond to the blending of the new feature and the standing shock. The observed bimodal distribution of the EVPAs could be due to the different polarimetric properties of the two components. A similar case was found in the core region of PKS 1510-089 during a γ-ray flare in 2015 (Park et al. 2019).

4.2. Testing the SMBBH Model

OJ 287 is one of the most promising candidates for harboring an SMBBH system at the center. In fact, OJ 287 is among the candidates for hosting a nano-Hz gravitational wave–emitting SMBBH system (Valtonen et al. 2021). The binary model has been successful in explaining the periodic light curves and predicting upcoming impact flares, which have been confirmed by observations within a few hours (e.g., Laine et al. 2020). The direction of the jet axis was also found to vary with time, and this could also be related to the orbital motion of the BHs (Dey et al. 2021). Models that do not require a secondary BH to explain the observed variability have also been proposed. For instance, the flux variation could be explained by viewing angle changes and the Doppler beaming effects of a precessing jet. The precession could be driven by the Lense–Thirring effect, due to misalignment between the BH spin and the accretion disk (e.g., Britzen et al. 2018; Liska et al. 2018; Chatterjee et al. 2020; Liska et al. 2021). It would also be possible for MHD instabilities (current-driven or Kelvin–Helmholtz) to produce a helical distorted jet structure (e.g.,

[38] In fact, the high X-ray flux of OJ 287 detected during the Swift MOMO program triggered the VHE observations, which led to the first VHE detection.

Mizuno et al. 2012; Perucho et al. 2012; Vega-García et al. 2019).

Dey et al. (2021) established a model to explain the parsec-scale jet direction variations at different frequencies, in which the jet precession is powered by the SMBBH with parameters constrained by optical observations. This model predicts that the 86 GHz jet axis should be $\sim -37^{\circ}$ around 2017 April, assuming a disk model. The PAs of the inner jet components (e.g., C1 and C2a) measured in our GMVA + ALMA observations agree well with this prediction (see Table 1). However, we note that this agreement is partially due to the observing epoch being not far apart from the 86 GHz GMVA data used to constrain the model. Furthermore, this agreement will not rule out other possible scenarios. For example, the tilted accretion could also result in the precession of the inner jet. Britzen et al. (2018) argue that the PA change observed at 15 GHz can be modeled by a jet precession combined with a nutation of the axis. The precession could be a result of Lense–Thirring effects, and a secondary BH is not always required. Furthermore, our RML images also revealed a twisted pattern of the innermost jet, which resembles a precessing jet in projection.

Future kinematic studies with multi-epoch GMVA and EHT observations will hopefully provide further insights to distinguish among different theoretical models regarding the underlying nature of the source.

Dey et al. (2021) also explored the possibility of the existence of a jet from the secondary SMBH based on the SMBBH model. With the high sensitivity and improved north–south resolution resulting from the participation of ALMA, we found no evidence for a secondary jet, even in the `eht-imaging` and `SMILI` images with super-resolution. There could be several possible reasons for such a nondetection. First, the jet is likely to be short-lived, as commented upon in Dey et al. (2021). Since the projected separation of the two SMBHs in 2017 April is $\sim$10 μas (Dey et al. 2018), the current image resolution is not sufficient to spatially resolve the binary system if there is no extended jet emission from the secondary SMBH. The same would apply if the secondary jet extends in a similar direction as the primary jet. If the secondary jet is present and points in a different direction, the nondetection implies that the brightness temperature of the jet must be lower than 4×10^9 K, which corresponds to three times the r.m.s. level of the `eht-imaging` map. We note that the dynamic range of our image reconstruction is much higher than the mass ratio of the two BHs.

We further note that the GMVA + ALMA observations presented in this work are part of a multiwavelength observing campaign of OJ 287. Close-in-time observations with the EHT at 230 GHz (on 2017 April 4 and 9) and with the RadioAstron space-VLBI mission at 22 GHz (on 2017 March 7) could provide even higher angular resolutions and probe slightly different regions of the inner jet. Together with the observations at X-ray and optical bands (e.g., Komossa et al. 2017, 2020, 2021a, 2021b, 2021c), we will be able to test or obtain constraints on the physical parameters of the possible jet associated with the secondary SMBH.

5. Summary

We carried out GMVA + ALMA observations of OJ 287 on 2017 April 2, which are the first VLBI observations with the phased ALMA. The improved north–south resolution and array sensitivity, together with the newly developed RML methods, have enabled us to obtain high-fidelity super-resolved images of the OJ 287 jet with unprecedentedly high angular resolution. The convolved RML images also agree with the CLEAN reconstruction. The images have revealed a twisted structure in the innermost region of the jet. Our result suggests that the C0 component lying at the southeastern end of the jet is more likely the VLBI core, as it is bright, compact, and relatively depolarized. The C2 component located at $\sim$200 μas northwest of the core shows a conical morphology and complex substructures in polarization. We argue that this component could be an oblique or recollimation shock, or related to a traveling component passing through a stationary feature in the jet. We have also carried out the first attempt to search for a jet from the secondary BH, as proposed by Dey et al. (2021), based on the SMBBH model. The nondetection could be due to the small projected separation, the short lifetime, or a difference in the physical conditions of the secondary jet. The EHT and RadioAstron observations carried out in 2017 and later could provide further tests of the SMBBH model.

The work at the IAA-CSIC is supported in part by the Spanish Ministerio de Economía y Competitividad (grants AYA2016-80889-P and PID2019-108995GB-C21), the Consejería de Economía, Conocimiento, Empresas y Universidad of the Junta de Andalucía (grant P18-FR-1769), the Consejo Superior de Investigaciones Científicas (grant 2019AEP112), and the State Agency for Research of the Spanish MCIU through the "Center of Excellence Severo Ochoa" award to the Instituto de Astrofísica de Andalucía (SEV-2017-0709). This publication acknowledges the project M2FINDERS, which is funded by the European Research Council (ERC) under the European Union's Horizon 2020 research and innovation program (grant agreement No. 101018682). L.L. acknowledges the support of the DGAPA/PAPIIT grants IN112417 and IN112820, the CONACyT-AEM grant 275201, and the CONACyT-CF grant 263356. T.S. was supported by the Academy of Finland projects 274477, 284495, 312496, and 315721. Y.K. was supported in the framework of the State project "Science" by the Ministry of Science and Higher Education of the Russian Federation, under the contract 075-15-2020-778. J.Y.K acknowledges support from the National Research Foundation of Korea (grant no. 2022R1C1C1005255). R.-S. L is supported by the Max Planck Partner Group of the MPG and the CAS, the Key Program of the National Natural Science Foundation of China (grant No. 11933007), the Key Research Program of Frontier Sciences, CAS (grant No. ZDBS-LY-SLH011), and the Shanghai Pilot Program for Basic Research – Chinese Academy of Science, Shanghai Branch (JCYJ-SHFY-2022-013).

This paper makes use of the following ALMA data: ADS/JAO.ALMA#2016.1.01116.V. ALMA is a partnership of ESO (representing its member states), NSF (USA), and NINS (Japan), together with NRC (Canada), MOST and ASIAA (Taiwan), and KASI (Republic of Korea), in cooperation with the Republic of Chile. The Joint ALMA Observatory is operated by ESO, AUI/NRAO, and NAOJ. The ALMA data required nonstandard processing by the VLBI QA2 team (C. Goddi, I. Martí-Vidal, G. B. Crew, H. Rottmann, and H. Messias). This work is partially based on observations with the 100-m telescope of the MPIfR (Max-Planck-Institut für Radioastronomie) at Effelsberg. This research has made use

of data obtained with the Global Millimeter VLBI Array (GMVA), which consists of telescopes operated by the MPIfR, IRAM, Onsala, Metsähovi, Yebes, the Korean VLBI Network, the Greenland Telescope, the Green Bank Observatory (GBT), and the Very Long Baseline Array (VLBA). The VLBA and the GBT are facilities of the National Science Foundation, operated under a cooperative agreement by Associated Universities, Inc. The data were correlated at the correlator of the MPIfR in Bonn, Germany.

Facilities: ALMA, GMVA, VLBA, GBT, EVN, Effelsberg, Metsähovi Radio Observatory, Onsala Space Observatory, IRAM-30 m RT, Yebes-40 m RT.

Software: AIPS (Greisen 2003), DiFX (Deller et al. 2007), `DIFMAP` (Shepherd et al. 1995), `eht-imaging` (Chael et al. 2018), `ParselTongue` (Kettenis et al. 2006), `SMILI` (Akiyama et al. 2017), `Altair` (VanderPlas et al. 2018), `Vega-Lite` (Satyanarayan et al. 2017).

Appendix
Calibration of the Instrumental Polarization

Calibration of the instrumental polarization leakage (also known as the D-terms) is required to obtain reliable polarimetric maps of the target. Each of the two pipelines that we used to perform polarimetric imaging (see Section 2) has independently implemented this calibration step.

The LPCAL pipeline loads the self-calibrated visibility data and the CLEAN Stokes I image of OJ 287 produced by `DIFMAP` and runs the AIPS task LPCAL to solve for the D-terms. LPCAL assumes that the source can be divided into a few subcomponents, each with a constant fractional polarization. LPCAL solves the D-terms for each IF independently; the results are shown in the top left panel of Figure 7. We have flagged the stations that only have data for one circular polarization (Yebes-40m) and stations that show low S/N on cross-hands (RL and LR) polarization data (VLBA North Liberty and Onsala).

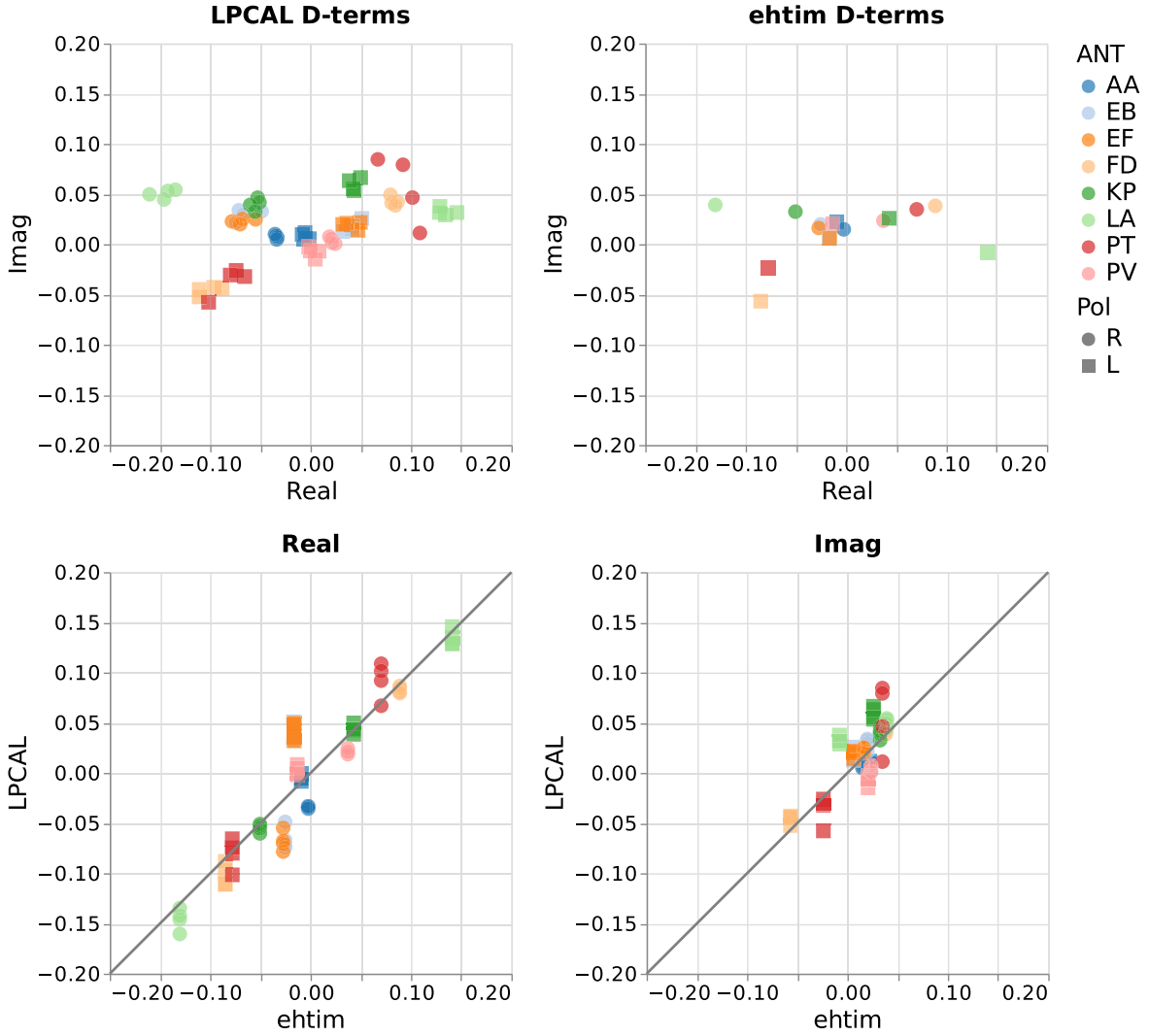

Figure 7. Top: D-terms solutions for each station obtained with LPCAL (left) and `eht-imaging` (right). LPCAL solves for each of the four IFs independently, while in `eht-imaging` the data for different IFs are averaged. Bottom: comparison of the real (left) and imaginary (right) components of the D-terms solutions between `eht-imaging` (*x*-axis) and LPCAL (*y*-axis). In all panels, the circular and square symbols represent the data for right-handed circular polarization and LCP, respectively. The solutions for the different stations are plotted in different colors. The abbreviations stand for the following station names, as follows: AA: ALMA; EB: Effelsberg (RDBE); EF: Effelsberg (DBBC2); FD: VLBA Fort Davis; KP: VLBA Kitt Peak; LA: VLBA Los Alamos; PT: VLBA Pie Town; and PV: IRAM-30 m.

On the other hand, the `eht-imaging` pipeline performs the instrumental polarization calibration in parallel with the imaging of the polarimetric data products. The pipeline computes the leakage terms by minimizing the difference between the self-calibrated data and the sampled data from the corrupted reconstructions. For details of the polarimetric imaging with `eht-imaging`, refer to Chael et al. (2016). The `eht-imaging` software by default averages the data at different IFs, so we have flagged the stations that show large differences in D-terms across IFs (VLBA BR and OV) in our polarimetric analysis. The `eht-imaging` results are shown in the top right panel of Figure 7.

Despite the different approaches to solving instrumental leakages, the two pipelines provide very consistent results in terms of the D-terms estimation, as shown in the bottom panels of Figure 7, which validate our polarization calibration. The absolute calibration of the EVPA was obtained by comparison with the ALMA observations of OJ 287 at the same frequency performed during the same observation campaign (Goddi et al. 2021).

ORCID iDs

Guang-Yao Zhao https://orcid.org/0000-0002-4417-1659
José L. Gómez https://orcid.org/0000-0003-4190-7613
Antonio Fuentes https://orcid.org/0000-0002-8773-4933
Thomas P. Krichbaum https://orcid.org/0000-0002-4892-9586
Efthalia Traianou https://orcid.org/0000-0002-1209-6500
Rocco Lico https://orcid.org/0000-0001-7361-2460
Ilje Cho https://orcid.org/0000-0001-6083-7521
Eduardo Ros https://orcid.org/0000-0001-9503-4892
S. Komossa https://orcid.org/0000-0002-9214-4428
Kazunori Akiyama https://orcid.org/0000-0002-9475-4254
Keiichi Asada https://orcid.org/0000-0001-6988-8763
Lindy Blackburn https://orcid.org/0000-0002-9030-642X
Silke Britzen https://orcid.org/0000-0001-9240-6734
Gabriele Bruni https://orcid.org/0000-0002-5182-6289
Geoffrey B. Crew https://orcid.org/0000-0002-2079-3189
Rohan Dahale https://orcid.org/0000-0001-6982-9034
Lankeswar Dey https://orcid.org/0000-0002-2554-0674
Roman Gold https://orcid.org/0000-0003-2492-1966
Sara Issaoun https://orcid.org/0000-0002-5297-921X
Michael Janssen https://orcid.org/0000-0001-8685-6544
Svetlana Jorstad https://orcid.org/0000-0001-6158-1708
Jae-Young Kim https://orcid.org/0000-0001-8229-7183
Jun Yi Koay https://orcid.org/0000-0002-7029-6658
Yuri Y. Kovalev https://orcid.org/0000-0001-9303-3263
Shoko Koyama https://orcid.org/0000-0002-3723-3372
Andrei P. Lobanov https://orcid.org/0000-0003-1622-1484
Laurent Loinard https://orcid.org/0000-0002-5635-3345
Ru-Sen Lu https://orcid.org/0000-0002-7692-7967
Sera Markoff https://orcid.org/0000-0001-9564-0876
Alan P. Marscher https://orcid.org/0000-0001-7396-3332
Iván Martí-Vidal https://orcid.org/0000-0003-3708-9611
Yosuke Mizuno https://orcid.org/0000-0002-8131-6730
Jongho Park https://orcid.org/0000-0001-6558-9053
Tuomas Savolainen https://orcid.org/0000-0001-6214-1085
Teresa Toscano https://orcid.org/0000-0003-3658-7862

References

Agudo, I., Marscher, A. P., Jorstad, S. G., et al. 2012, ApJ, 747, 63
Akiyama, K., Ikeda, S., Pleau, M., et al. 2017, AJ, 153, 159
Blandford, R. D., & Payne, D. G. 1982, MNRAS, 199, 883
Blandford, R. D., & Znajek, R. L. 1977, MNRAS, 179, 433
Boccardi, B., Krichbaum, T. P., Ros, E., & Zensus, J. A. 2017, A&ARv, 25, 4
Britzen, S., Fendt, C., Witzel, G., et al. 2018, MNRAS, 478, 3199
Broderick, A. E., & McKinney, J. C. 2010, ApJ, 725, 750
Cawthorne, T. V. 2006, MNRAS, 367, 851
Cawthorne, T. V., & Cobb, W. K. 1990, ApJ, 350, 536
Cawthorne, T. V., Jorstad, S. G., & Marscher, A. P. 2013, ApJ, 772, 14
Chael, A. A., Johnson, M. D., Bouman, K. L., et al. 2018, ApJ, 857, 23
Chael, A. A., Johnson, M. D., Narayan, R., et al. 2016, ApJ, 829, 11
Chatterjee, K., Younsi, Z., Liska, M., et al. 2020, MNRAS, 499, 362
Chiaberge, M., Celotti, A., Capetti, A., & Ghisellini, G. 2000, A&A, 358, 104
Cohen, M. H. 2017, Galax, 5, 12
Deller, A. T., Tingay, S. J., Bailes, M., & West, C. 2007, PASP, 119, 318
Dey, L., Valtonen, M. J., Gopakumar, A., et al. 2021, MNRAS, 503, 4400
Dey, L., Valtonen, M. J., Gopakumar, A., et al. 2018, ApJ, 866, 11
Event Horizon Telescope Collaboration, Akiyama, K., Alberdi, A., et al. 2019a, ApJL, 875, L2
Event Horizon Telescope Collaboration, Akiyama, K., Alberdi, A., et al. 2019b, ApJL, 875, L4
Fromm, C. M., Perucho, M., Mimica, P., & Ros, E. 2016, A&A, 588, A101
Fromm, C. M., Perucho, M., Ros, E., Savolainen, T., & Zensus, J. A. 2015, A&A, 576, A43
Fromm, C. M., Ros, E., Perucho, M., et al. 2013a, A&A, 557, A105
Fromm, C. M., Perucho, M., Ros, E., et al. 2011, A&A, 531, A95
Fromm, C. M., Ros, E., Perucho, M., et al. 2013b, A&A, 551, A32
Fuentes, A., Gómez, J. L., Marti, J. M., & Perucho, M. 2018, ApJ, 860, 121
Fuentes, A., Torregrosa, I., Martí, J. M., Gómez, J. L., & Perucho, M. 2021, A&A, 650, A61
Goddi, C., Martí-Vidal, I., Messias, H., et al. 2019, PASP, 131, 075003
Goddi, C., Martí-Vidal, I., Messias, H., et al. 2021, ApJL, 910, L14
Gómez, J. L., Marti, J. M., Marscher, A. P., & Ibanez, J. M. 1997, VA, 41, 79
Gomez, J. L., Marti, J. M. A., Marscher, A. P., Ibanez, J. M. A., & Marcaide, J. M. 1995, ApJL, 449, L19
Gómez, J. L., Lobanov, A. P., Bruni, G., et al. 2016, ApJ, 817, 96
Gómez, J. L., Traianou, E., Krichbaum, T. P., et al. 2022, ApJ, 924, 122
Greisen, E. W. 2003, in Information Handling in Astronomy - Historical Vistas, Vol. 285, ed. A. Heck (Dordrecht: Kluwer), 109
Hodgson, J. A., Krichbaum, T. P., Marscher, A. P., et al. 2017, A&A, 597, A80
Honma, M., Akiyama, K., Uemura, M., & Ikeda, S. 2014, PASJ, 66, 95
Jorstad, S. G., Marscher, A. P., Morozova, D. A., et al. 2017, ApJ, 846, 98
Kettenis, M., van Langevelde, H. J., Reynolds, C., & Cotton, B. 2006, in ASP Conf. Ser. 351, Astronomical Data Analysis Software and Systems XV, ed. C. Gabriel et al. (San Francisco, CA: ASP), 497
Komossa, S., Grupe, D., Gallo, L. C., et al. 2021a, ApJ, 923, 51
Komossa, S., Grupe, D., Parker, M. L., et al. 2020, MNRAS, 498, L35
Komossa, S., Grupe, D., Schartel, N., et al. 2017, in IAU Symp. 324, New Frontiers in Black Hole Astrophysics, ed. A. Gomboc (Cambridge: Cambridge Univ. Press), 168
Komossa, S., Grupe, D., Kraus, A., et al. 2021b, Univ, 7, 261
Komossa, S., Grupe, D., Parker, M. L., et al. 2021c, MNRAS, 504, 5575
Kuramochi, K., Akiyama, K., Ikeda, S., et al. 2018, ApJ, 858, 56
Laine, S., Dey, L., Valtonen, M., et al. 2020, ApJL, 894, L1
Lee, S.-S., Lobanov, A. P., Krichbaum, T. P., et al. 2008, AJ, 136, 159
Lehto, H. J., & Valtonen, M. J. 1996, ApJ, 460, 207
Lico, R., Casadio, C., Jorstad, S. G., et al. 2022, A&A, 658, L10
Liska, M., Hesp, C., Tchekhovskoy, A., et al. 2018, MNRAS, 474, L81
Liska, M., Hesp, C., Tchekhovskoy, A., et al. 2021, MNRAS, 507, 983
Lister, M. L., & Homan, D. C. 2005, AJ, 130, 1389
Lobanov, A. 2015, A&A, 574, A84
Martí-Vidal, I., Roy, A., Conway, J., & Zensus, A. J. 2016, A&A, 587, A143
Mizuno, Y., Gómez, J. L., Nishikawa, K.-I., et al. 2015, ApJ, 809, 38
Mizuno, Y., Lyubarsky, Y., Nishikawa, K.-I., & Hardee, P. E. 2012, ApJ, 757, 16
Mukherjee, R. & VERITAS Collaboration 2017, ATel, 10051, 1
Nair, D. G., Lobanov, A. P., Krichbaum, T. P., et al. 2019, A&A, 622, A92
Park, J., Lee, S.-S., Kim, J.-Y., et al. 2019, ApJ, 877, 106
Perucho, M., Kovalev, Y. Y., Lobanov, A. P., Hardee, P. E., & Agudo, I. 2012, ApJ, 749, 55
Porth, O., Fendt, C., Meliani, Z., & Vaidya, B. 2011, ApJ, 737, 42
Readhead, A. C. S. 1994, ApJ, 426, 51
Rioja, M., & Dodson, R. 2011, AJ, 141, 114
Rioja, M., Dodson, R., Gómez, J., et al. 2017, Galax, 5, 9
Satyanarayan, A., Moritz, D., Wongsuphasawat, K., & Heer, J. 2017, IEEE Trans. Vis. Comput. Graph., 23, 341
Shepherd, M. C., Pearson, T. J., & Taylor, G. B. 1995, BAS, 27, 903
Sillanpää, A., Haarala, S., Valtonen, M. J., Sundelius, B., & Byrd, G. G. 1988, ApJ, 325, 628

Stickel, M., Fried, J. W., & Kuehr, H. 1989, A&AS, 80, 103
Tateyama, C. E., & Kingham, K. A. 2004, ApJ, 608, 149
Thompson, A. R., Moran, J. M., & Swenson 2017, Interferometry and Synthesis in Radio Astronomy (3rd edn.; Cham: Springer)
Tingay, S. J., Reynolds, J. E., Tzioumis, A. K., et al. 2002, ApJS, 141, 311
Valtonen, M. J., Ciprini, S., & Lehto, H. J. 2012, MNRAS, 427, 77
Valtonen, M. J., Lehto, H. J., Takalo, L. O., & Sillanpää, A. 2011, ApJ, 729, 33
Valtonen, M. J., Nilsson, K., Sillanpää, A., et al. 2006, ApJL, 643, L9
Valtonen, M. J., Lehto, H. J., Nilsson, K., et al. 2008, Natur, 452, 851
Valtonen, M. J., Zola, S., Ciprini, S., et al. 2016, ApJL, 819, L37
Valtonen, M. J., Dey, L., Gopakumar, A., et al. 2021, Galax, 10, 1
VanderPlas, J., Granger, B., Heer, J., et al. 2018, JOSS, 3, 1057
Vega-García, L., Perucho, M., & Lobanov, A. P. 2019, A&A, 627, A79
Weaver, Z. R., Jorstad, S. G., Marscher, A. P., et al. 2022, ApJS, 260, 12
Zhao, G.-Y., Algaba, J. C., Lee, S. S., et al. 2018, AJ, 155, 26